The Astronomical Journal, 163:87 (12pp), 2022 February https://doi.org/10.3847/1538-3881/ac41c4

Direction-dependent Corrections in Polarimetric Radio Imaging. III. A-to-Z Solver—Modeling the Full Jones Antenna Aperture Illumination Pattern

Srikrishna Sekhar[1,2,3], Preshanth Jagannathan[2], Brian Kirk[2], Sanjay Bhatnagar[2], and Russ Taylor[1,3]
[1] Inter-University Institute for Data Intensive Astronomy, and Department of Astronomy, University of Cape Town, Cape Town, South Africa
[2] National Radio Astronomy Observatory, 1003 Lopezville Road, Socorro, NM 87801, USA
[3] Inter-University Institute for Data Intensive Astronomy, and Department of Astronomy, University of the Western Cape, Bellville, South Africa; srikrishna@idia.ac.za
Received 2021 July 6; revised 2021 December 3; accepted 2021 December 3; published 2022 January 25

Abstract

In this third paper of a series describing direction-dependent corrections for polarimetric radio imaging, we present the the A-to-Z solver methodology to model the full Jones antenna aperture illumination pattern (AIP) using Zernike polynomials. In order to achieve accurate, thermal noise-limited imaging with modern radio interferometers, it is necessary to correct for the instrumental effects of the antenna primary beam (PB) as a function of time, frequency, and polarization. The algorithm employs the orthonormal, circular Zernike polynomial basis to model the full Jones AIP response, which is obtained by a Fourier transform of corresponding antenna holography measurements. These full Jones models are then used to reconstruct the full Mueller AIP response of an antenna, in principle accounting for all the off-axis frequency-dependent leakage effects of the PB. The A-to-Z solver is general enough to accommodate any interferometer for which holographic measurements exist, and we have successfully modeled the AIP of the VLA, MeerKAT, and ALMA as a demonstration of its versatility. We show that our models capture the PB morphology to high accuracy within the first two side lobes, and show the viability of full Mueller gridding and deconvolution for any telescope given high-quality holographic measurements.

Unified Astronomy Thesaurus concepts: Astronomical techniques (1684); Polarimetry (1278); Aperture synthesis (53); Radio astronomy (1338); Radio interferometry (1346)

1. Introduction

Modern radio interferometers are capable of high-sensitivity imaging in a high dynamic range. Imaging in particular is limited by the presence of direction-dependent effects (DDEs). In general, DDEs are a function of direction, frequency, time, and polarization and are typically corrected for during the imaging process, unlike direction-independent effects (DIEs). Following Hamaker et al. (1996), the measurement equation in radio interferometry is of the form

$$\boldsymbol{V}_{\rm ij}^{\rm Obs} = \mathsf{G}_{\rm ij} \int \mathsf{M}_{\rm ij}(\boldsymbol{s}) \boldsymbol{I}_{\rm ij}(\boldsymbol{s}) e^{i\boldsymbol{b}_{\rm ij}\cdot\boldsymbol{s}} d\boldsymbol{s} \tag{1}$$

for a single baseline *i*–*j* for a given frequency at a given time, $\mathsf{G}_{\rm ij}$ are the DIEs, $\mathsf{M}_{\rm ij}$ are the DDEs, $\boldsymbol{I}_{\rm ij}$ is the sky brightness distribution, $\boldsymbol{s}$ defines the direction vector on the sky, and $\boldsymbol{b}_{\rm ij}$ are the uv coordinates of the baseline *i*–*j*. All the terms within the integral in the above equation have to be corrected for during the imaging process, as they are all functions of the direction vector $\boldsymbol{s}$.

$\mathsf{M}_{\rm ij}$ is a 4×4 matrix describing the direction-dependent (DD) mixing of the full-polarization image 4-vector ($I_{\rm pp}$, $I_{\rm pq}$, $I_{\rm qp}$, and $I_{\rm qq}$). Each element of $\mathsf{M}_{\rm ij}$ is a description of the DD response of an interferometer. The diagonal elements represent the power response (*i.e.,* forward gain) of the interferometer. Elements in the first row (or column) encode the first-order DD polarization leakages due to antenna optics. Other off-diagonal elements encode higher-order combinations of power and polarization leakage terms. These are typically orders of magnitude smaller (but not always). Accurate models for the elements of $\mathsf{M}_{\rm ij}$, particularly the leakage terms, are a prerequisite for full Mueller imaging that corrects for the effects of the antenna DD response in full polarization. This work describes a method to develop a model for $\mathsf{M}_{\rm ij}$ based on holographic measurements of the antenna response.

The Mueller matrix $\mathsf{M}_{\rm ij}$ can be written as

$$\mathsf{M}_{\rm ij}(\boldsymbol{s}, \nu, t) = \mathsf{J}_i(\boldsymbol{s}, \nu, t) \otimes \mathsf{J}_j^*(\boldsymbol{s}, \nu, t), \tag{2}$$

where $\otimes$ is the Kronecker product, and J_i and J_j are the antenna voltage patterns or the DD Jones matrices for antennas i and j, respectively, as a function of frequency ν and time t. The antenna Jones matrix encodes the polarization response of an antenna-to-incident radiation and is represented by a 2×2 matrix given by

$$\mathsf{E} = \begin{pmatrix} E_p & -E_{p\leftarrow q} \\ E_{q\leftarrow p} & E_q \end{pmatrix} \tag{3}$$

for two orthogonal feed polarizations p and q.

In order to accurately reconstruct the sky brightness distribution, it is necessary to remove the imprint of $\mathsf{M}_{\rm ij}$ for each baseline for all directions, frequency, and time.

Formally, the primary beam (PB) of an antenna is given by the Fourier transform of the aperture illumination pattern (AIP) and can be represented as

$$\mathsf{A}_i(u, v, \nu, t) = \mathcal{F}\mathsf{J}_i(\boldsymbol{s}, \nu, t), \tag{4}$$

where A_i is the complex AIP of antenna i at uv coordinates u and v. J_i is the measured complex image plane Jones matrix, (

i.e., antenna voltage pattern), and $\mathcal{F}$ is the Fourier transform operator. A_i is mathematically a finite, bounded function, and correspondingly, J_i is unbounded. The AIP in general is a function of time, frequency, and polarization. The time dependence for an altitude-azimuth mounted antenna manifests as a rotation of the source within the field of view. We can consider measurements made by a radio interferometer as the sampling of a continuous visibility coherence function by the AIPs at the locations of the baselines in the *uv*-plane. The measurement equation (Equation (1)) can be recast using Equation (4) (following Bhatnagar et al. 2013) as

$$\boldsymbol{V}_{\rm ij}^{\rm Obs}(\boldsymbol{s},\,\nu,\,\theta_{\rm PA}) = \mathsf{A}_{\rm ij}(\boldsymbol{s},\,\nu,\,\theta_{\rm PA}) \circledast \boldsymbol{V}_{\rm ij}^{\rm True} \tag{5}$$

,where $\mathsf{A}_{\rm ij} = \mathcal{F}\mathsf{M}_{\rm ij}$ is the AIP (given by the Fourier transform of Equation (1)), $\circledast$ is the outer convolution operator (as described in Bhatnagar et al. 2013), $\theta_{\rm PA}$ is the parallactic angle, and $\boldsymbol{V}_{\rm ij}^{\rm True} = \mathcal{F}\boldsymbol{I}_{\rm ij}(\boldsymbol{s})$ is the continuous true-sky coherence function that is sampled by the baseline AIP $\mathsf{A}_{\rm ij}$, resulting in the observed visibility data given by $\boldsymbol{V}_{\rm ij}^{\rm Obs}$.

Various algorithms are used to mitigate the effect of DDEs such as peeling and facet-based algorithms (e.g., Cotton et al. 2004; Noordam 2004; Intema 2009; Van Weeren et al. 2016) and projection algorithms (e.g., Bhatnagar et al. 2008, 2013; Cornwell et al. 2008; Tasse et al. 2013; Van der Tol et al. 2018), both of which require a model of either the PB or the AIP (we refer to Rau et al. 2009 for more details).

In this paper, we restrict ourselves to a discussion of PB correction via projection algorithms, specifically, A-projection. However, we note that the A-to-Z solver modeling approach is itself agnostic to the choice of imaging algorithm. Although we create the models in the aperture (*i.e.,* data) domain, a Fourier transform is sufficient to provide equivalent models for image-domain algorithms.

The A-projection algorithm applies an a priori model inverse of the antenna AIP $\mathsf{A}_{\rm ij}^{M\dagger}/|\mathsf{A}_{\rm ij}|^2$ at the time of convolutional gridding such that

$$\mathcal{F}^{\dagger}\left[\frac{\mathsf{A}_{\rm ij}^{M\dagger}}{|\mathsf{A}|^2}\right] * \boldsymbol{V}_{\rm ij}^{\rm Obs} = \mathcal{F}^{\dagger}[\boldsymbol{V}_{\rm ij}^{\rm True}] = \boldsymbol{I}_{\rm ij} \tag{6}$$

.

The resulting image is free of the time, frequency, and polarization DDEs of the baseline *i*–*j*. The DDEs are "projected out" by using a gridding convolution function that is equal to the inverse of the model AIP, thus recovering the true-sky brightness distribution. The quality of the model and its inverse then determines how well we can correct for the DDE of the baseline AIP. There have been many different approaches to fitting, modeling, and simulating the antenna PB response at different observatories (e.g., Du et al. 2016; Sokolowski et al. 2017; Jagannathan et al. 2018; Asad et al. 2021). The primary challenge of pure modeling approaches such as electromagnetic simulations or ray tracing lie with determining the off-diagonal (leakage) Jones response of the antenna. Capturing these leakage terms is necessary to be able to perform accurate wide-field polarimetric observations. In all cases, and particularly for dish antennas, measuring the antenna Jones beams via holographic measurements yields the "ground truth" of the antenna Jones response.

We approach the problem in the data domain where we model the bounded and finite AIP (Bates 1971; Scott & Ryle 1977). We also restrict our discussions to radio interferometers composed of dishes for the rest of the paper, specifically focusing on the Karl. G. Jansky Very Large Array (VLA; Perley et al. 2011), the Atacama Large Millimeter Array (ALMA; Wootten 2003), and MeerKAT (Jonas & Team 2018). We present here a new method, the A-to-Z solver, to derive a Zernike polynomial based model of the AIP from measurements of antenna holography and demonstrate its accuracy and efficacy in modeling the full Jones response of the antenna. This allows us in turn to generate full Mueller AIP and antenna PB models. This paves the way for a full Mueller treatment of A-projection, which will result in accurate wide-field, wide-band off-axis polarimetry. This is currently under development and will be described in an upcoming paper (P. Jagannathan et al., 2021, in preparation). This paper and the next is a part of our effort to implement full Mueller polarization corrections in the A-Projection algorithm in CASA (McMullin et al. 2007).

The rest of the paper is organized as follows: Section 2 provides the details of how we go from Jones measurements in the image domain to Zernike polynomial models of the aperture. Section 3 discusses the results of the modeling, the accuracy and reproducibility and so on, and Section 4 provides a summary of the methods and their merits and limitations.

2. From Apertures to Zernike

2.1. Interferometric Holography

Antenna holography is the process of measuring the far-field voltage pattern of an antenna (Bates 1971; Napier & Bates 1971), either by pointing at a reference (terrestrial) source or at a well-characterized celestial calibrator source. In order to measure the Jones matrices, a two-dimensional raster scan is performed around a known, unresolved, and preferably unpolarized calibrator source. Half the array tracks the calibrator source (the "tracking antennas"), while the other half performs the raster scan (the "scanning antennas"). The two halves are then swapped around, in order to obtain a measurement of all the antennas in the array.

We can recast Equation (1) in the following form (in vector notation) under the assumption that all the tracking antennas are pointing at the same location on the sky as

$$\boldsymbol{V}_{\rm st} = \mathsf{G}_{\rm st}\mathcal{F}[(\mathsf{J}_s \otimes \mathsf{J}_t^{\dagger})\mathsf{S}\boldsymbol{I}^{\rm sky}] \tag{7}$$

,where the subscripts s and t refer to the scanning and tracking antennas, respectively. $\mathsf{G}_{\rm st}$ are the direction-independent gains, and S is a transformation matrix that converts the sky brightness distribution from Stokes basis into the feed basis of measurement. The Jones matrices J_s and J_t represent the antenna far-field voltage patterns in feed basis of the scanning and the tracking antennas. After calibration of the tracking antennas is performed (using the point-source calibrator), the above equation reduces to

$$\boldsymbol{V}_{\rm st}^{\rm cal} = \mathcal{F}[(\mathsf{J}_s \otimes \mathbb{1})] \tag{8}$$

,where the J_t is reduced to the identity matrix 1, and we can therefore measure the complex Jones response (as a function of direction) of the scanning antennas from the calibrated visibilities. The product $\mathsf{S}\boldsymbol{I}^{\rm sky}$ is the calibrator source flux as measured in the feed basis. Since the calibrator flux is nominally well known, this becomes a constant (known) factor that can be normalized out.

Furthermore, correlation products from all the pairs of scanning-scanning antennas can be constructed, given by

$$\boldsymbol{V}_{\rm ss} = \mathsf{G}_{\rm ss}\mathcal{F}[(\mathsf{J}_{\rm si} \otimes \mathsf{J}^{\dagger}_{\rm sj})\boldsymbol{SI}^{\rm sky}] \quad (9)$$

,where $\mathsf{J}_{\rm si}$ and $\mathsf{J}_{\rm sj}$ are Jones beams corresponding to the baseline *i–j*. $\boldsymbol{V}_{\rm ss}$ then measures the total power Jones beam. These total power measurements measure the first row of the Mueller matrix. It is not possible to reconstruct the antenna Jones matrix from these Mueller measurements. However, the first row of the Mueller matrix can be reconstructed from the Jones beams (Equation (8)) and provides an internal consistency check for our measurements. We describe below the details of the holography for three different instruments (VLA, MeerKAT, and ALMA).

VLA—We use the holography data described in Perley (2016). In this paper, we discuss only the *S*-band observations, although the method is applicable to any observable frequency band at the VLA. At *S*-band the observations used 3C147 as the standard unpolarized calibrator. The scanning antennas covered a regular grid of 57×57 points around the calibrator, with an angular separation of $2\farcm62$ between each pointing. This was sufficient to sample out to five side lobes at the highest end of the band. Two spectral windows (centered at 2308 MHz and 2948 MHz) were badly affected by persistent radio frequency interference (RFI), and we could not obtain reasonable beam measurements from them. We instead used ray-traced antenna AIPs that were modeled in the same way as the rest of the band to derive the Zernike polynomial coefficients.

MeerKAT—We used MeerKAT *L*-band holography data that covered the entire MeerKAT *L*-band (from ∼880 to 1680 MHz) at a resolution of ∼0.85 MHz. The data sampled out to five side lobes at the highest frequency. The holographic pointing was performed in a spiral pattern around the calibrator source 3C273, using the on-the-fly capabilities of MeerKAT. The beams were then resampled onto a regular 128×128 grid with a separation of $4\farcm68$ per grid pointing. For more details, we refer to Asad et al. (2021).

ALMA—We use ALMA holography data described in Bhatnagar et al. (2020), obtained in 2018. We focus here only on the Band 3 data, which measured out to about the five side lobes of the PB. The holography sampled a 49×49 grid with a spacing of $0.2 \times$ half-power beam width (HPBW) around the calibrator source J1924–2914. The full Jones beams for both the 12m antennas, DA and DV, were recorded. The DA and DV antennas are two of the three types of 12 m antennas that constitute ALMA. The primary difference between the antennas is the position of the antenna feed legs, which are rotated by 45°.

2.2. Pointing Offset Correction

Prior to modeling the measured aperture, any residual pointing errors in the holography need to be removed first, as small pointing errors cause a phase gradient across the aperture (Bhatnagar & Cornwell 2017). If these phases remain during the modeling step, they will be captured by the Zernike model, leading to offsets in the generated model PB. While all the telescopes discussed here have some form of a priori models for pointing offsets (and in some cases perform a dedicated pointing calibration scan), residual pointing errors tend to accumulate through the course of an observation.

In order to measure and correct for the pointing errors, a 2D Gaussian is fitted to the main lobe of the holographic beams. We use a nonlinear Levenberg–Marquardt least-squares fitter (Moré 1978) as implemented in the `astropy` Python package (Robitaille et al. 2013).

The beam for each feed polarization was fitted independently, and the vector sum of the pointing vectors between the two feeds is taken to be the pointing offset. This procedure is repeated as a function of antenna and frequency. We use the vector sum to preserve the beam squint between the two orthogonal polarizations. The measured pointing offsets were used to regrid the beam such that the peak of the Stokes I beam lies at the center of the image. All four Jones beams are regridded identically. For the VLA and ALMA, where we had access to the holography visibility data, we were able to remove the pointing offsets per baseline prior to averaging all the baselines of an antenna. This results in a higher signal-to-noise ratio (S/N) upon averaging, eliminating smearing and decorrelation due to baseline-based pointing errors.

Finally, the holography data were averaged across all antennas and all channels within a spectral window prior to applying the Fourier transform. This averaging results in an improvement of $\sqrt{N_{\rm ant} \times N_{\rm chan}}$ in the S/N, which is especially useful in the cross hands, which usually have ∼10–100×low er S/N than the parallel hands. Empirically, we have determined that the average antenna model is sufficient for our modeling purposes. It is worth noting, however, that the choice to average across antennas and frequency will impose a dynamic range limitation on the final image, contingent on the level of antenna-to-antenna variations and variation across a single spectral window for a particular instrument.

2.3. Obtaining the AIP

The spatial frequency resolution in the aperture domain is inversely proportional to the total angular extent sampled by holography. It is given by

$$\Delta u \propto \frac{1}{l_{\rm sky}} \quad (10)$$

,where $l_{\rm sky}$ is the total angular extent of the holography (in radians), and Δu is the size of the resolution element in the aperture (in lambda).

It is necessary that a large number of side lobes be covered by holography in order to obtain accurate aperture plane measurements. However, in practice, only a finite number of side lobes can be measured because of various practical considerations. In this case, the corresponding aperture domain measurements are affected by ringing, and these ringing artifacts extend far beyond the physical aperture. We therefore need to determine the "true" edge of the aperture in order to model the AIP rather than the ringing artifacts.

The real part of the AIP for an unblocked aperture is guaranteed to be positive within the physical aperture itself. In the case of a blocked aperture, $\mathcal{R}(\mathsf{A})$ can have null or negative values within the regions that are shadowed. However, in both cases, the last pixel inside the aperture (in an unblocked region) will be positive and the first pixel outside the aperture will be negative. This is commonly called the "aperture roll-off". In absolute value, the drop between these two pixels can be a factor of between 10 and 100. At low frequencies, the magnitude of the drop is smaller because there is more diffraction and spill-over at the edge of the aperture. The above

condition has proven to be very robust in determining the cutoff radius of the aperture for a variety of different antenna types and frequencies. We identify the size of the aperture by locating the radius of the first negative component in the real part of the aperture, in a direction moving out from the center of the aperture. This condition is general and allows us to naturally determine the cutoff radius as a function of frequency.

The apertures derived from antenna holography have a gradual roll-off at the edge of the aperture due to the limited number of side lobes that can be sampled by holography. The diameter of the main lobe of the PB depends very strongly on the size of the aperture. To obtain the correct beam sizes, it is therefore necessary to determine the aperture size as accurately as possible. Directly applying a Fourier transform to the measured holography typically results in 5–6 pixels across the aperture, and the roll-off is contained in a single pixel. This can bake in an error of up to 15% in the derived PB size.

In order to obtain accurate (<1% error) PB sizes, we used an oversampling factor of 100 prior to the Fourier transform of the holography followed by image plane minimization (see Section 3.4) to account for the changing aperture efficiency across the band. We performed this interpolation in CASA using the `imregrid`[4] task, which performs cubic spline interpolation while preserving pixel flux scaling. We note here that interpolation of any kind does not increase the amount of information in the underlying image. Therefore interpolating by a large factor, while allowing us to determine the edge of the roll-off more accurately, does not increase the steepness of the roll-off or give us a higher resolution across other features in the aperture.

2.4. Aperture Fitting

Zernike polynomials are complex, orthonormal polynomials defined on a unit circle (Zernike 1934; Born & Wolf 2013). Zernike polynomials also form the natural basis to model optical apertures, making them an ideal fit for modeling the antenna AIP.

We refer to Lakshminarayanan & Fleck (2011) for the definition of the Zernike polynomials, but we use Noll sequential indices (Noll 1976) to map the two Zernike indices (n, m) to a single index k. Under this mapping, the first 10 orders ($n: 0 \rightarrow 10$) of Zernike polynomials map to the first 66 terms ($k: 0 \rightarrow 66$) of the flattened index.

We fit the aperture measurements with the first 10 orders (*i.e.,* 66 terms) of Zernike polynomials after first taking out the known systematic errors from the holography image (e.g., antenna pointing offsets).

The AIP model is given by

$$\mathsf{A}^M(\boldsymbol{s}) = \sum_{k=0}^{10} [\mathsf{A}_k^{\mathcal{R}} + \iota \mathsf{A}_k^{\mathfrak{I}}] \cdot Z(k, \boldsymbol{s}), \tag{11}$$

where $\boldsymbol{s}$ spans the aperture of a fixed diameter, and A_k are the coefficients for the kth Zernike term $Z(k, \boldsymbol{s})$. The superscripts $\mathcal{R}$ and $\mathfrak{I}$ indicate separate coefficients for the real and imaginary parts of the AIP. The objective functions used for deriving the coefficients $\mathsf{A}^{\mathcal{R}}$ and $\mathsf{A}^{\mathfrak{I}}$ are

$$\chi^2_{\mathcal{R}} = \sum_{\boldsymbol{s}} |\mathcal{R}[\mathsf{A}^H(\boldsymbol{s}) - \mathsf{A}^M(\boldsymbol{s})]|^2 \tag{12a}$$

$$\chi^2_{\mathfrak{I}} = \sum_{\boldsymbol{s}} |\mathfrak{I}[\mathsf{A}^H(\boldsymbol{s}) - \mathsf{A}^M(\boldsymbol{s})]|^2, \tag{12b}$$

where A^H is the measured AIP from holography observations. The models are fitted in the aperture domain independently for the real and imaginary parts and for each of the four Jones terms. Modeling all the terms of the complex antenna Jones matrix allows us to reconstruct the entire 4×4 Mueller matrix. The reverse operation of going from Mueller matrix to Jones matrices is not possible due to missing phase information in the measured Mueller matrix. This is the primary reason for the measurement of antenna Jones matrices (voltage beams).

We use a nonlinear least-squares fitter as implemented in the SciPy package (Virtanen et al. 2020) to minimize the objective functions defined in Equation (12). The fitter uses a nonlinear trust region solver algorithm (Branch et al. 1999) with a stopping threshold criterion. We define the stopping threshold to be equal to the thermal noise per pointing in order to prevent overfitting. We will demonstrate in the following sections that the correlated nature of our residuals, albeit small, is a sign of unmodeled Zernike terms. We eschew using higher orders in favor of accurately modeling the main lobe of the antenna PB and the first side lobe.

The plots in Figure 1 show the fitted power per Zernike term (real and imaginary) for the VLA and MeerKAT. The y-scale on the plots is in arbitrary units. The distribution of power across the Zernike terms reflects the different characteristics of the two apertures. The VLA has a blocked aperture and feed legs that cast a shadow on the dish. Modeling the relatively sharp edges of the shadow on the aperture requires higher-order Zernike terms. Accordingly, the high spatial frequency Zernike terms (above index 50) see an increase in power for the case of the VLA, as seen in Figure 1. In contrast, MeerKAT has an unblocked aperture and correspondingly has lower amplitudes for the higher-order terms.

As mentioned previously, the Zernike polynomials capture various physically meaningful optical properties of the aperture (such as the piston, tip, tilt, etc.). Figure 2 plots the Z_2^{-2} term, or the "oblique astigmatism", across a section of the band for the VLA and MeerKAT. This term clearly captures the resonant frequency-dependent variation between the feed and the antenna surface for both the telescopes. We measure the VLA standing wave of frequency ∼17 MHz, corresponding to a subreflector at a height of ∼8.5 m consistent with known values for the VLA (e.g., Jagannathan et al. 2018). For MeerKAT, we measure a standing wave with a frequency of ∼37 MHz, corresponding to a subreflector height of ∼4 m, which is also consistent with the MeerKAT specification (Esterhuyse et al. 2011).

Figure 3 shows a plot of the measured aperture, the Zernike model, and the residual for (a) the VLA, (b) MeerKAT, (c) ALMA DV, and (d) ALMA DA. The plots show the magnitude (*i.e.,* $\sqrt{\mathcal{R}(\mathsf{A}^M)^2 + \mathfrak{I}(\mathsf{A}^M)^2}$ following Equation (12)) of the aperture for a single polarization and frequency for each telescope type. As noted earlier, the fitting is performed independently for the real and imaginary components. The broad morphology of the aperture is captured by the model, leaving behind residuals at the percent level or lower in all cases. The residuals correspond to the unmodeled higher spatial frequency signal and look similar across frequency and polarization for all the telescopes.

[4] https://casa.nrao.edu/casadocs/casa-6.1.0/global-task-list/task_imregrid/about

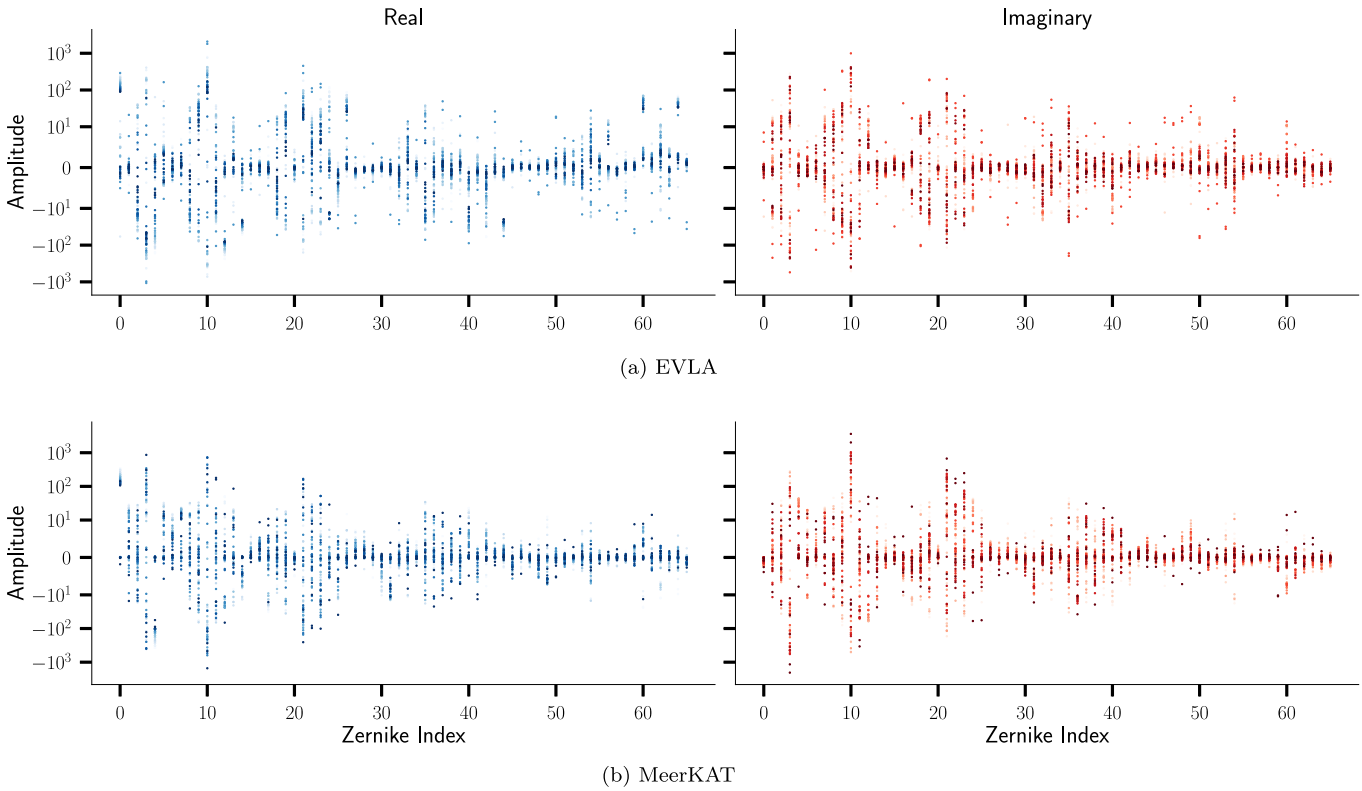

Figure 1. Plot of the power per Zernike term for the real and imaginary parts of the AIP for EVLA (top) and MeerKAT (bottom). The y-axis scale is in arbitrary units because the FFT to convert the Jones beams into apertures scales all the pixels by a factor of $\sqrt{N_{\rm pix}}$. This is has no impact on the accuracy of the modeling or reconstruction because the relative power between the different Zernike terms determines the morphology of the reconstructed aperture, and this is a conserved quantity under this transformation.

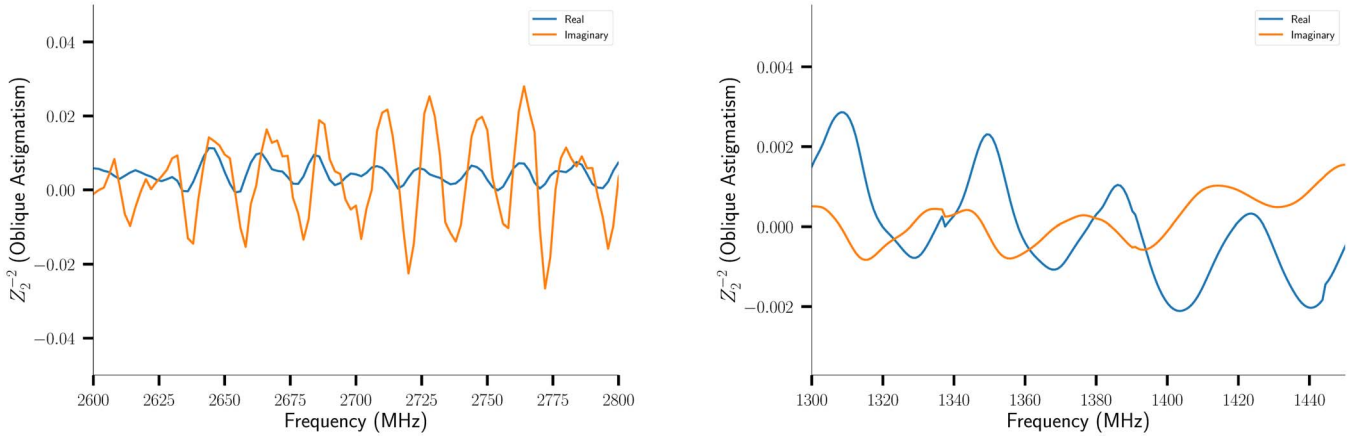

Figure 2. Normalized fitted value of Z_2^{-2} (oblique astigmatism) from the VLA and MeerKAT apertures. The sinusoidal patterns present in these coefficients correspond to the standing waves in the antenna. Left: the coefficient power across a section of the VLA S-band. The coefficients capture the standing wave of ∼17 MHz. Right: the coefficient power across a section of the MeerKAT L-band. The standing wave with a frequency of ∼37 MHz is captured. These standing waves correspond to the secondary reflection between the antenna surface and the feed.

Figure 4 shows a slice across the residuals of the different antenna types discussed in this paper. The shaded region spans the region from the first null to the fourth null, *i.e.,* the first three side lobes for the EVLA. These plots are the Fourier transform of the aperture residuals, *i.e.,* $\mathcal{F}[\mathsf{A}^{\rm Holo} - \mathsf{A}^{M}]$, because the modeling is performed in the aperture domain. The beam models capture the response to floating point precision (10^{-6}) out to the second side lobe for all the modeled telescopes. The residual error rapidly increases as we move farther out, which is expected. In Figure 4 the residuals correspond to unmodeled power in the outer side lobes. The higher-order side lobes correspond to the high spatial frequency features in the aperture domain, which correspondingly require higher-order Zernike polynomials to model. Empirically, we see that increasing the number of terms used to model the aperture results in a reduction in the systematics of the aperture plane residuals.

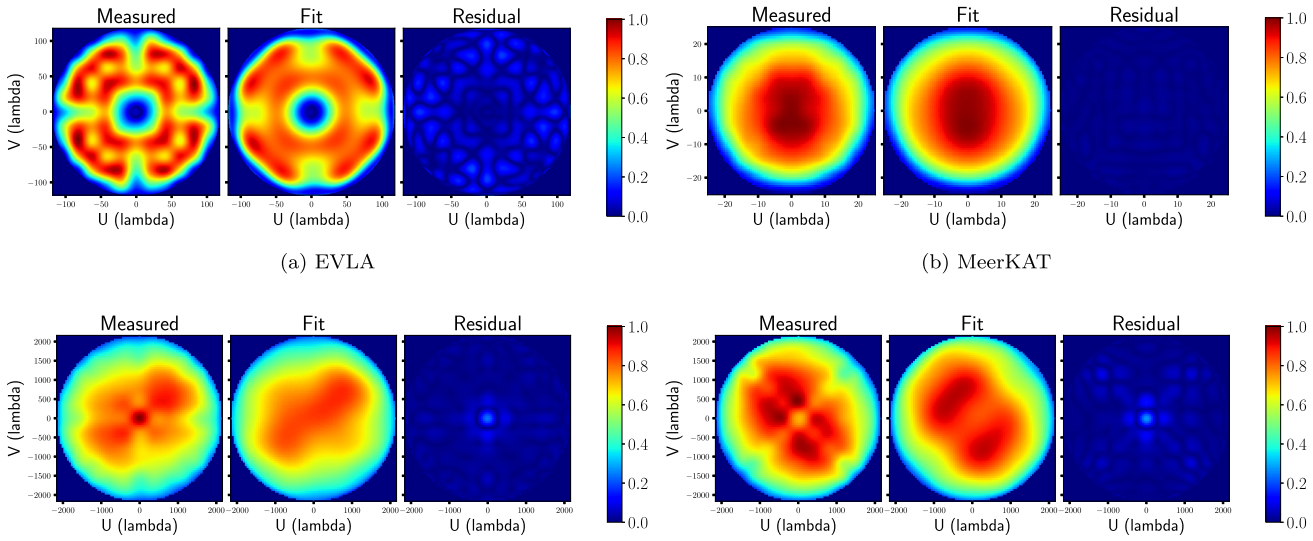

(a) EVLA (b) MeerKAT

(c) ALMA DV (d) ALMA DA

Figure 3. The measured, modeled, and residual apertures for each of the four antenna types discussed in this paper. In all cases, only the amplitude term for a single polarization is shown for brevity. The residuals look similar across polarization in all cases. (a) VLA *S*-band (3 GHz) R polarization, (b) MeerKAT *L*-band (1.2 GHz) X polarization, (c) ALMA Band 3 (108 GHz) DV-type X polarization, and (d) ALMA Band 3 (108 GHz) DA-type X polarization. The apertures have been normalized to the peak illumination value. In every case, the residuals show systematic higher-order structure that corresponds to power in the higher side lobes. With the current level of modeling, we are able to capture all the power in the main lobe and in the first side lobe.

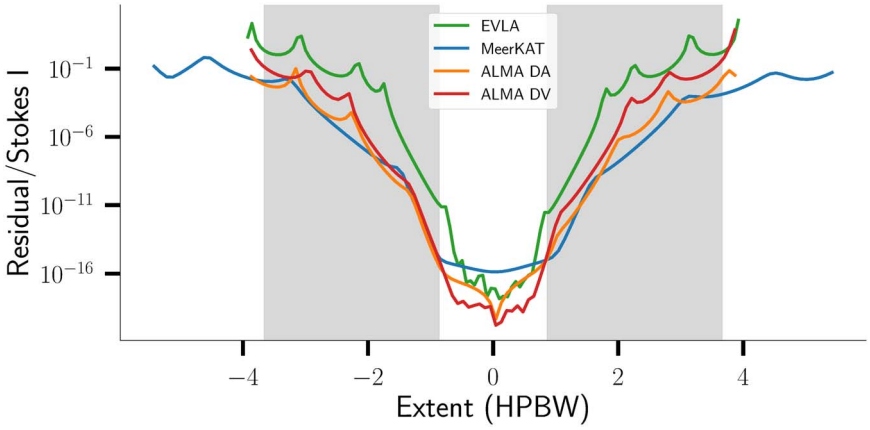

Figure 4. Cut across the normalized residual PB for each of the four antenna types discussed here. The plot shows where the unmodeled structure in the aperture appears in the image plane. The MeerKAT beam is at 1.6 GHz, the VLA *S*-band at 4 GHz, and the ALMA beams are at 108 GHz. In the case of the VLA and MeerKAT, we selected the highest SPW in order to show the largest number of side lobes. The shaded region spans the region from the first null through the fourth null, *i.e.,* the first three side lobes for the EVLA.

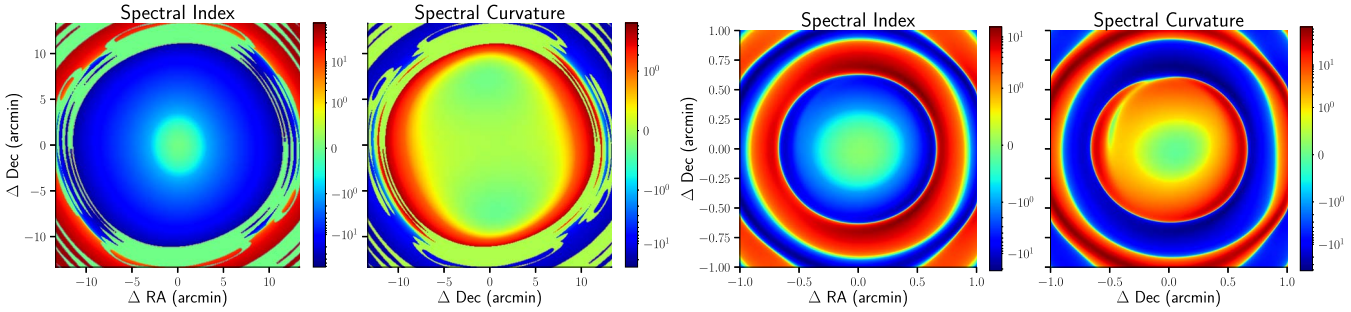

(a) EVLA (a) MeerKAT

Figure 5. Plot of the spectral index and spectral curvature of the EVLA *S*-band (left) and MeerKAT *L*-band (right) beams. The plots show only the main lobes of the PB, with the spectral index steepening as we move farther away from the pointing center.

3. Results and Beam Properties

3.1. Beam Spectral Index

With modern interferometers, wide-band continuum imaging has become the norm, enabling theoretically higher sensitivies. In order to achieve these sensitivity limits, it is vital to account for the effects of the wide-band antenna PB. Figure 5 shows the spectral index $\alpha_{\rm pb}$ and the spectral curvature $\beta_{\rm pb}$ introduced by the antenna PB onto a wide-band continuum image at 3 GHz at the VLA on the left panel and at 1.2 GHz of MeerKAT on the right. The spectral index and curvature are defined as

$$\boldsymbol{I}_{\nu} = \boldsymbol{I}_{\nu_0}\left(\frac{\nu}{\nu_0}\right)^{\alpha+\beta\log\left(\frac{\nu}{\nu_0}\right)} \tag{13}$$

,where α and β are the spectral index and spectral curvature, respectively, $\boldsymbol{I}$ is the source flux density at frequency ν, and ν_0 is the reference frequency.

The uncorrected PB spectral index at half-power of the VLA PB is $\alpha_{\rm pb} = -5$. The various means of mitigating the PB spectral index have been analyzed in detail in Rau et al. (2016). It is worth noting that for large continuum frequency bands of observations, the higher-order spectral terms of the PB such as curvature also leave a significant spectral signature on the PB across wide fields of view.

3.2. Beam Squint and Squash

Figure 6 shows the contour density plots of the measured residual pointing errors for EVLA, MeerKAT, and the ALMA DA and DV antennas. The errors plotted here were determined independently per antenna, spectral window (SPW), and channel, except for ALMA, for which the band averaged values for a single SPW were used. In all cases each color corresponds to one of the two orthogonal feeds (blue shows R and X, and red represents L and Y). The VLA shows a clear separation between the pointing centers of the R and L feeds, corresponding to the well-known beam squint as demonstrated in Jagannathan et al. (2018). Both MeerKAT and ALMA show significant overlap between the pointing center of the feeds, as is expected from basic antenna optics for linear and circular feeds.

Figure 7 plots the frequency dependence of the mean squint and the beam squash. The mean pointing offset for each correlation is defined as

$$d_{\rm offset}(\nu) = \frac{1}{N_{\rm ant}}\sum_i \frac{\Delta\alpha_i(\nu) + \Delta\delta_i(\nu)}{2}, \tag{14}$$

where $\Delta\alpha_i(\nu)$ and $\Delta\delta_i(\nu)$ are the R.A. and decl. offsets, respectively, as a function of frequency. The beam squash is defined as

$$\Phi = \frac{\overline{l_{\rm major}}}{\overline{l_{\rm minor}}} \tag{15}$$

,where $\overline{l_{\rm major}}$ and $\overline{l_{\rm minor}}$ are the major and minor axes of the ellipse fitted to the beam of the antenna-averaged response in feed basis, measured along the position angle of the ellipse. The plot only shows the frequency dependence for VLA and MeerKAT because they have a large fractional bandwidth.

The VLA shows a clear separation between the pointing centers of the R and L feeds (Figure 7(1a)). The separation is ∼3% of the HPBW as a function of frequency, which is consistent with previous measurements of the beam squint. MeerKAT, however, shows a more complex beam squint behavior across the band. Both the X and Y feeds are biased toward positive offsets at lower frequencies and approach minimum at ∼1400 MHz. The beam squint also shows a quasi-oscillatory behavior. The periodicity of the oscillation does not correspond to the standing-wave frequency, and the cause of the quasiperiodicity of the pointing is not immediately obvious. In terms of beam squash, the VLA shows a consistent behavior across the band. There is a small amount of beam ellipticity ($\Phi = 1.01$–1.03) that slightly increases toward the higher frequencies. The MeerKAT beam squash behavior is analogous to the beam squint, the two feeds showing ellipticity along orthogonal directions, with a minimum at ∼1400 MHz.

3.3. Direction-dependent Polarization Leakage

During the process of antenna holography, we obtained two independent measurements of the antenna beams. The first are the Jones beams, as we discussed in previous sections. The second are the total power beams (see Equations (7) and (9)). Constructing the Stokes beams from the total power beams is a much more straightforward process and is identical to constructing the Stokes products from the correlated visibilities themselves. By comparing the full Stokes beams derived from Zernike models to the total power beams, we are able to verify both the efficacy of the Jones modeling against an independent measurement and the sign conventions of the Jones to Mueller unitary conversion matrix S (Hamaker et al. 1996). The conversion from Jones to Mueller via the unitary matrix S is given by

$$\mathsf{M}_{\rm stokes} = \mathsf{S}^{\dagger}[\mathsf{J}_i \otimes \mathsf{J}_j]_{\rm feed}\,\mathsf{S} \tag{16}$$

,where S is a 4×4 transformation matrix, and J_i and J_j are the 2×2 Jones matrices for antennas i and j, respectively.

Figure 8 shows the measured, modeled, and residual VLA *S*-band and ALMA Band 3 Stokes products. The top row shows the measured Stokes products from the total power beams. The second row shows the equivalent Zernike models of the beams, and the bottom row shows the difference between the two. The residuals in Stokes I are at the level of 10^{12}, i.e., a ∼1% fractional error on the beam model. The morphologies for the Stokes-Q and -U beams are generally in agreement. We note that the power beams are different from the Jones beams in two ways: *(i)* the baseline pairs used to construct the two sets of beams are different (and do not overlap), and *(ii)* the effect of pointing errors will affect the two beams slightly differently. The comparison with the power beams or the Mueller matrix does not reflect the efficacy of the fit itself, but rather demonstrates the internal consistency of the Jones matrices and the transformation matrix required to go from the feed to the Stokes basis, namely the S matrix.

As an additional consistency check, we compare the Stokes I PB generated from AW project to the Stokes I PB from holography. The AW project calculates the PB via a Fourier transform of the gridded, weighted baseline AIP derived during imaging, which is reflective of the true PB of the measurement.

Figure 9 shows the fractional residuals between the Stokes I beam produced by the `awproject` gridder in CASA and the Stokes I beam derived from the holography for the VLA at 2.8 GHz and MeerKAT at 1.25 GHz. This figure is representative of other SPWs across the band for both telescopes. The fractional error is large toward the nulls, which is expected. The

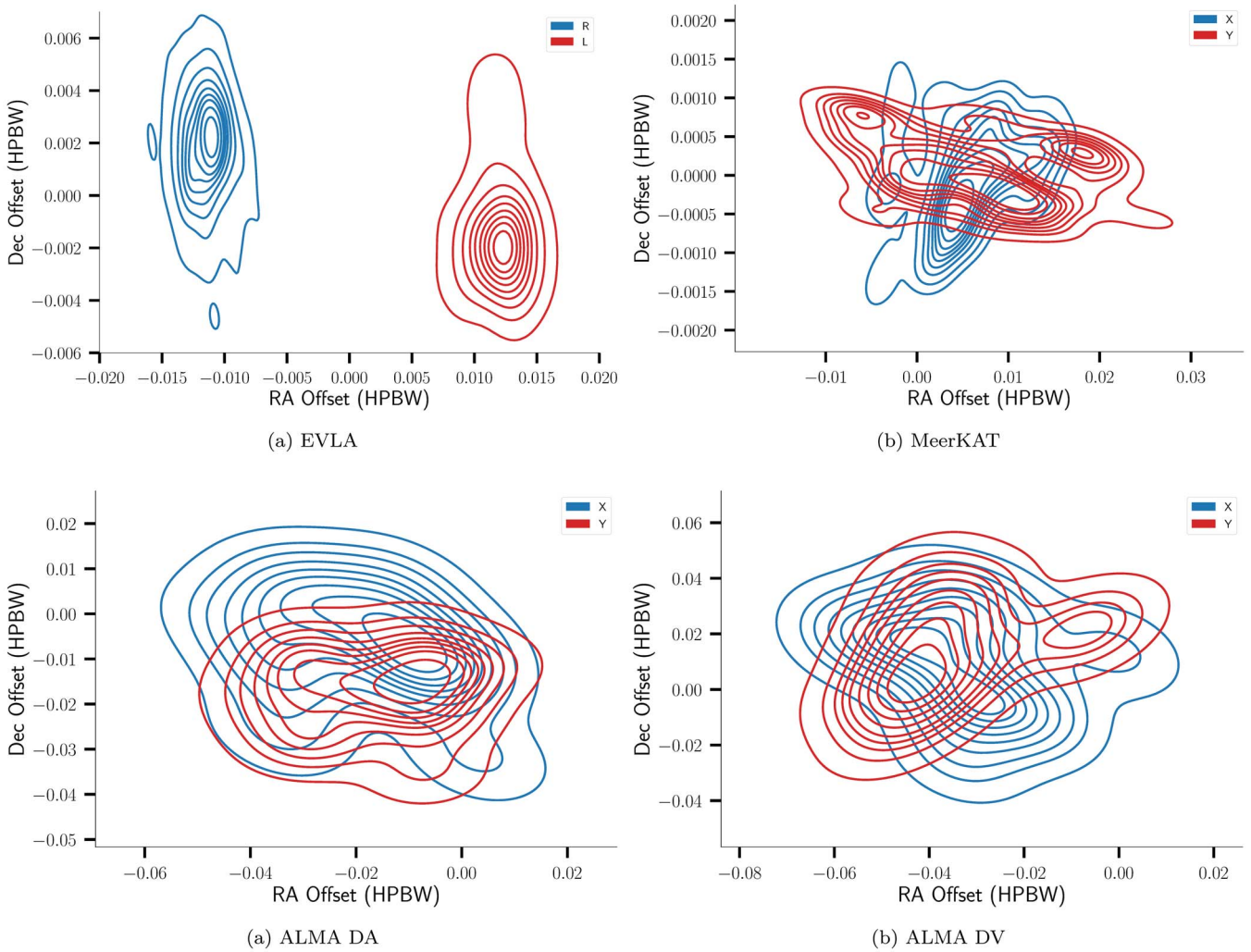

(a) EVLA (b) MeerKAT

(a) ALMA DA (b) ALMA DV

Figure 6. Contour density plots of the measured pointing offsets for the VLA, MeerKAT, and ALMA DA and DV. In all cases, the two different colors correspond to the different correlation products. The VLA is the only antenna type with circular feeds, and it shows a clear separation between the pointing centers of the R and L feeds. This separation is the well-known beam squint. The squint as a function of frequency is plotted in Figure 7. MeerKAT and ALMA both have linear feeds and do not show a consistent separation between the two feeds.

AW projection code as yet cannot perform full Mueller corrections, and hence we restrict ourselves to comparing the Stokes I beams. From these plots, it is clear that our modeling has captured the PB response well, both in the main lobe and the first (few) side lobe(s). The details of how these coefficients are included in CASA are outlined in Appendix B. The implementation of a full Mueller, wide-band AW projection algorithm is currently being tested, the results of which will be described in a forthcoming paper (Jagannathan et al., 2021, in preparation).

3.4. Modeling the Aperture across Frequency

In order to obtain PB sizes accurate to <1%, we need to account for changes in aperture efficiency across the band. Aperture efficiency changes the effective diameter of the dish, and we introduce a scaling factor η_A to account for this as follows:

$$D_A'(\nu) = \eta_A(\nu) D_A, \tag{17}$$

where D_A is the nominal antenna diameter (25 m in the case of the VLA), and D_A' is the effective antenna diameter. Figure 10 plots the behavior of η_A as a function of frequency for VLA *S*-band observations.

We derive this scaling factor in the following manner: *(i)* η_A is introduced in the code as a specifiable (free) parameter. *(ii)* For a given value of η_A, a PB image is generated (at a given frequency) using the `awproject` gridder in CASA, and the residuals are computed against the PB generated via the `standard` gridder. The value of η_A that minimizes these residuals is stored. We found that a brute-force minimization method was sufficient for generating a PB to the accuracy we required. To this end, at every η_A starting from 0.7 through 1.3 in steps of 0.01, the minimization was carried out. Further reducing the step size to 0.001 yielded no improvement in the values of η_A.

3.5. Efficacy

To show the performance of the Zernike modeled apertures in imaging, we carried out a simulation. We generated a sky model of six point sources, each with a flux density of 1 Jy, which were then attenuated by the average measured holographic antenna PB, using a central frequency of 2948

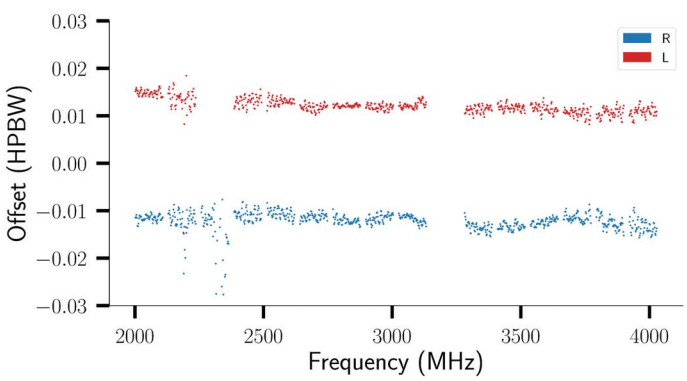

(1a) EVLA Mean Offset

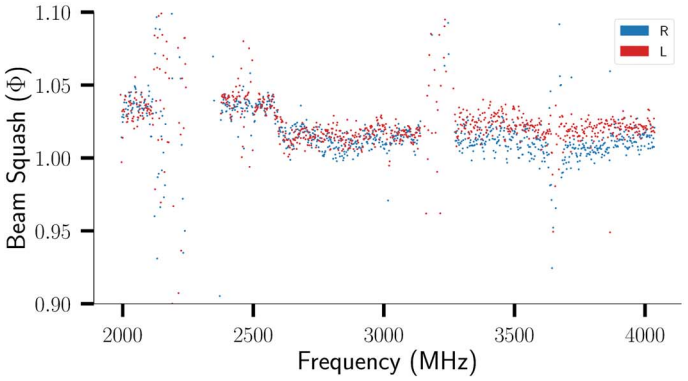

(1b) EVLA Squash

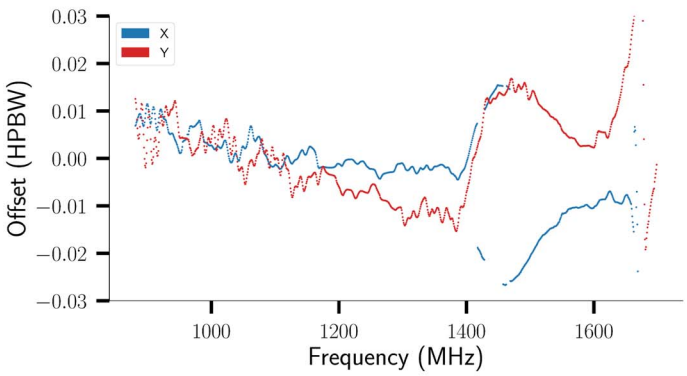

(2a) MeerKAT Mean offset

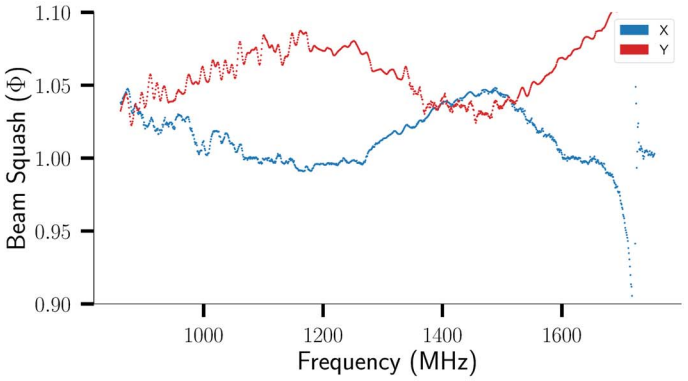

(2b) MeerKAT Squash

Figure 7. Plots of the mean pointing offset (left) and the beam squash (right) per correlation product as a function of frequency for EVLA and MeerKAT. These data show the frequency dependence of the same offsets as plotted in Figure 6. (1) The VLA shows a clear separation between the R and L feeds, which corresponds to ∼3% of the beam width as a function of frequency. This is consistent with previous measurements of the beam squint for the VLA. On the other hand, although the VLA PB shows some degree of ellipticity ($\Phi > 1$), the R and L beams are very similar across the band, and do not show a large difference in their beam squash. (2) MeerKAT has a more complex beam squint behavior vs. frequency. Both the X and Y feeds tend toward a zero mean offset at higher frequencies, with a minimum at ∼1400 MHz. The X and Y beams show a significantly different beam squash, indicating that the beams are preferentially elongated along orthogonal axes. Similarly to the squint, the beam squash is minimum at ∼1400 MHz.

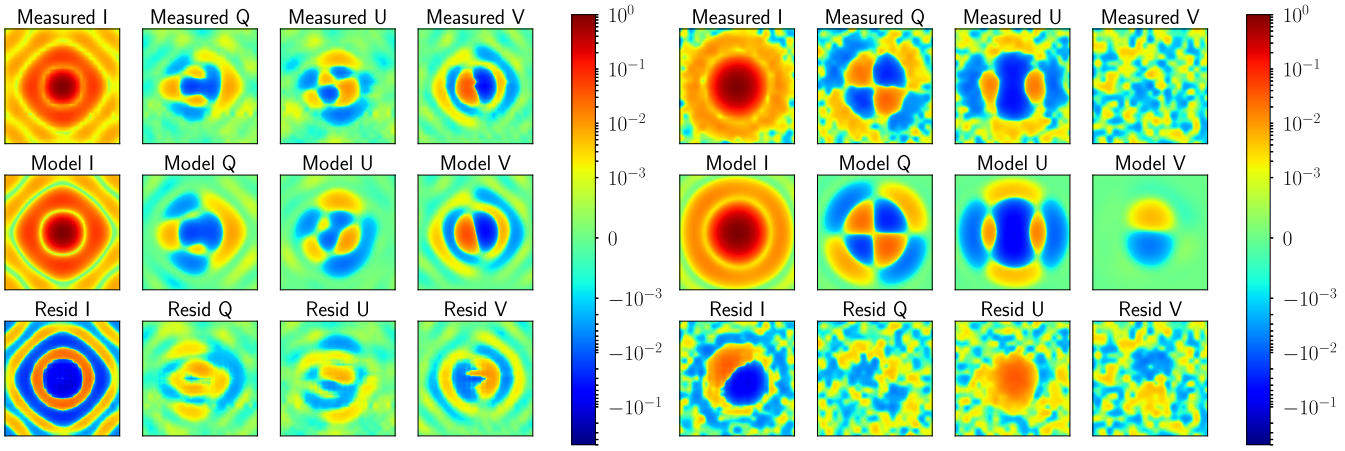

(a) EVLA

(b) ALMA DA

Figure 8. The full Mueller residuals for the VLA (left) and ALMA (right). In each figure we show from top to bottom the measured Stokes beams (total power), the model Stokes beams, and the residual. There is good agreement between the morphology of the measured and modeled Stokes beams. For ALMA, the Stokes V measurement has a very low S/N because it is the difference between the cross-hand feeds. We note that this is a problem only in the total power measurements; the S/N of the Jones beams is better.

MHz and 64MHz bandwidth. The simulated measurement set is generated following Jagannathan et al. (2017).

The sources were placed at PB gain locations of 1.0, 0.8, 0.5, 0.2, 0.1, and 0.05. The first five sources were placed in the main lobe, and the last source was placed at the peak of the first

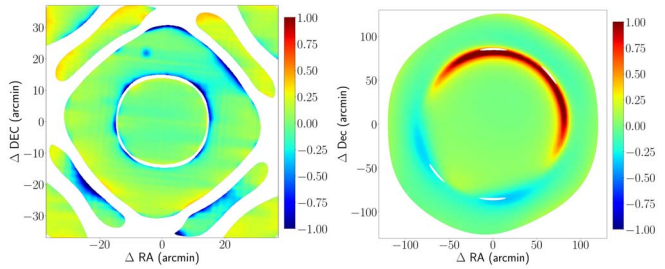

(a) EVLA (b) MeerKAT

Figure 9. Fractional residual between the Stokes I PB produced by the AW projection framework and the Stokes I PB generated from measured holography for the VLA at 2.9 GHz (left) and MeerKAT at 1.25 GHz (right). In both cases, the fractional error is $\leqslant$2% within the main lobe, rising to $\leqslant$10% in the first side lobe. The fractional error near the nulls will naturally tend to be very large.

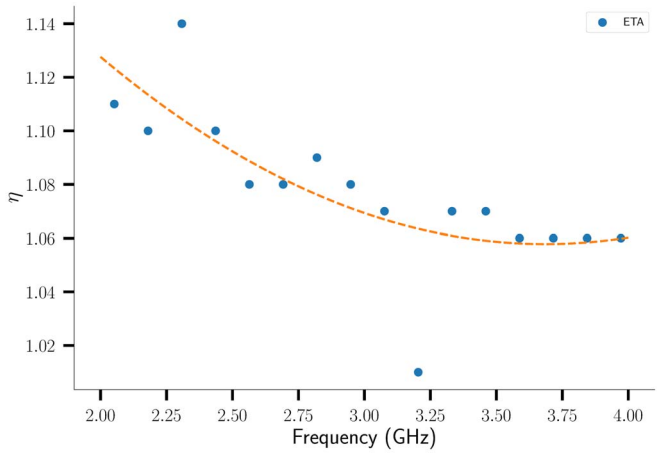

Figure 10. Plot of η_A scaling factor as a function of frequency for the VLA *S*-band. The dashed line is the polynomial fit to the data. We find that η_A reduces as a function of frequency, analogous to the increasing aperture efficiency, and flattens out at the highest frequencies. The sudden spike at $\sim$2.25 GHz and the dip at $\sim$3.25 GHz correspond to SPWs corrupted by RFI, yielding unreliable antenna holography measurements.

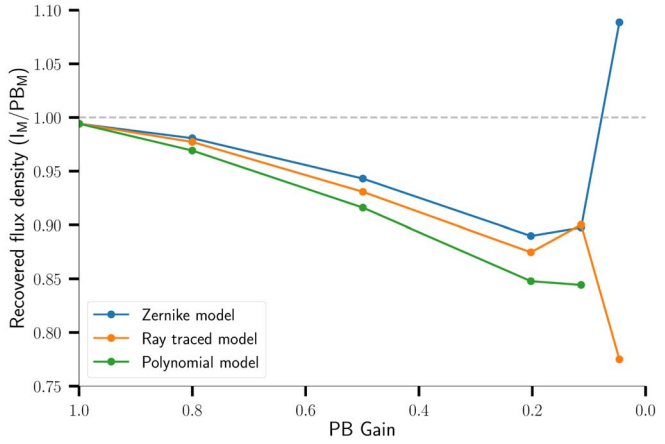

Figure 11. Plot of the recovered flux between the Zernike model, the ray-traced model, and the polynomial model of the EVLA PB.

side lobe. The resulting measurement set was then imaged using the `awproject` and `standard` gridding algorithms in CASA, and the resulting images were PB-corrected to recover the true flux densities, *i.e.*, $\boldsymbol{I_M/PB_M}$, where $\boldsymbol{I_M}$ is the recovered sky model, and $\boldsymbol{PB_M}$ is the antenna PB produced by the imaging algorithm during imaging.

Figure 11 shows the recovered flux densities of the sources as a function of the PB gain level. The dashed line in gray represents the true flux density of the predicted sources. If the recovery were exact, all points would lie along that line. The blue line represents the new Zernike aperture models used in AW projection, while the orange line represents ray-traced aperture illumination models currently in use. The green line plots the polynomial model of the antenna main lobe used by the default gridding algorithm (*i.e.,* the `standard` gridder) within the CASA `tclean` framework. The figure demonstrates that the Zernike polynomial model more accurately represents the antenna holography and consequently retrieves the flux density of the source across the main lobe and out to the first side lobe better, where the error in the retrieved flux density is 10%. The ray-traced AIP performance within the main lobe is consistently lower by 2% across the main lobe, but underestimates the flux density by nearly 23% at the first side lobe. The improvements in modeling the side lobe, as well as the ability to generate full Mueller PB models, is the primary advantage of the method outlined in this paper. The level of flux density recovery makes the A-to-Z solver a more versatile and effective method than both ray tracing and using axis-symmetric 2D polynomials, as demonstrated here.

4. Conclusion

We have demonstrated the A-to-Z solver methodology, which we used to model the full Jones response of an antenna using Zernike polynomials. We have further demonstrated that this approach results in wide-field, wide-band full Mueller PB models that are accurate to the first side lobe. By using the measured AIP, we rely on direct measurements of the optical properties to inform the modeling, which is necessary to capture the polarization leakage behavior. This makes it easy to generalize our method to any arbitrary interferometer with holographic measurements, without needing to rely on setting up complex simulations that typically require a large time investment and high computing capacities. We have demonstrated the generality of our approach by modeling the VLA, ALMA, and MeerKAT telescopes, which have a variety of different feed polarization, dish, and frequency configurations. The only limitation to extending this method to other telescopes and facilities is the availability of high-quality interferometric observations.

We also demonstrate the efficacy of the Zernike polynomials in modeling optical properties of the dish and beam, such as the standing wave due to the second reflection between the antenna feed and secondary reflector. These effects show up in different Zernike terms that typically correspond to actual optical aberrations such as the tip, tilt, defocus, and astigmatism. The broadband beam squint and beam squash behavior are also well modeled, and our measurements are consistent with existing previous estimates. The PB models described in this paper are generally accurate to one to two side lobes, which is relevant for wide-field imaging and deep mosaicing experiments.

We have implemented the A-to-Z modeling functionality in a Python package (Sekhar & Jagannathan 2021a)[5] that (at the time of writing) has been verified to work on the VLA L- and *S*-bands, MeerKAT *L*-band, and ALMA Band 3 data. These

[5] https://gitlab.nrao.edu/pjaganna/zcpb

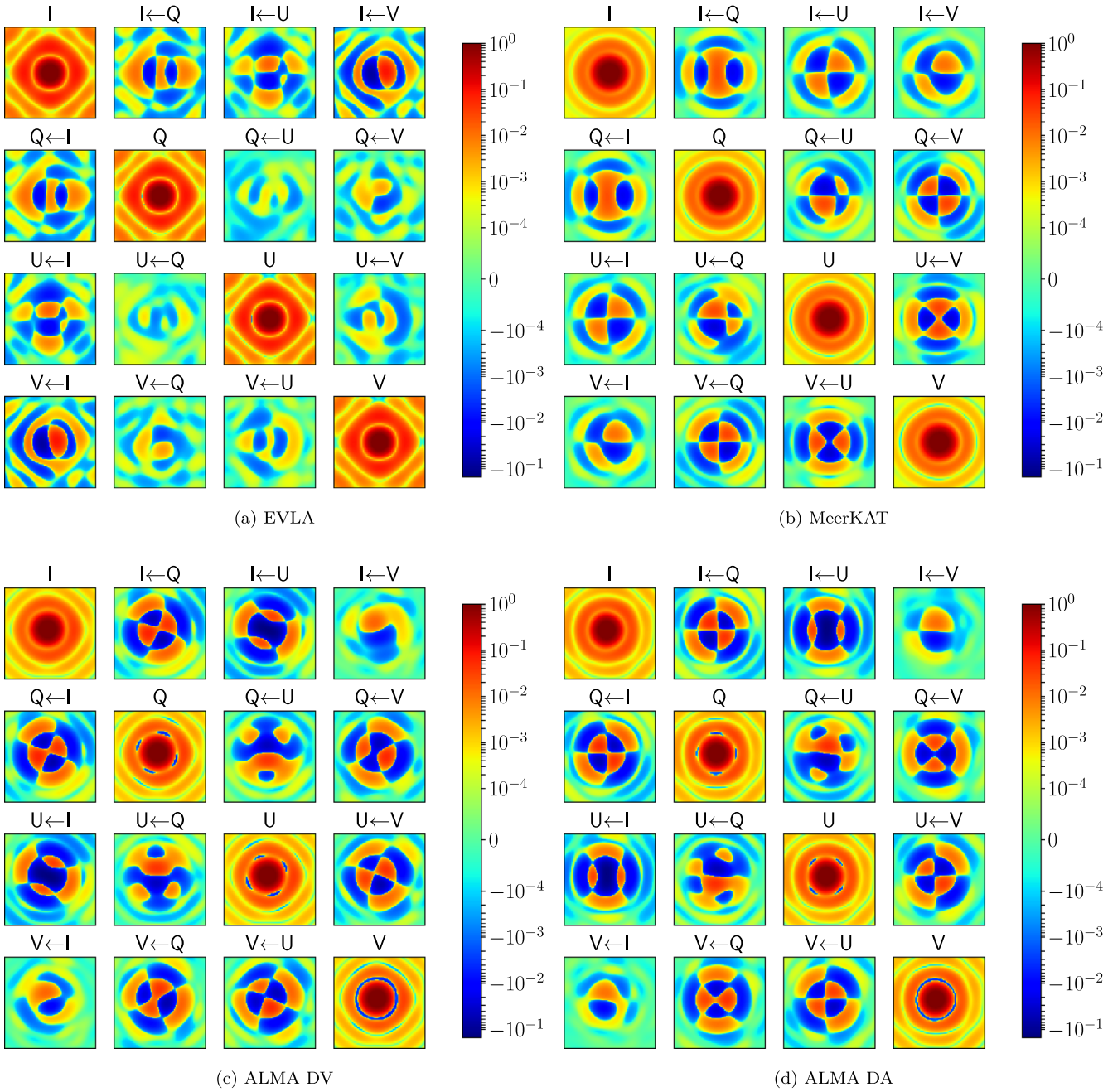

(a) EVLA (b) MeerKAT

(c) ALMA DV (d) ALMA DA

Figure 12. The DD Mueller terms generated from the Zernike models for (a) the VLA *S*-band (2.5 GHz), (b) the MeerKAT *L*-band (1.2 GHz), (c) ALMA DV antenna Band 3 (108 GHz), and (d) ALMA DA antenna Band 3 (108 GHz).

models can then be used to generate full Stokes beam models (*i.e.,* the first row of the Mueller matrix), the functionality for which has been implemented in a separate Python package (Sekhar & Jagannathan 2021b)[6] in order to perform image plane leakage corrections. These coefficients have also been included in (at the time of writing) a development branch of CASA that uses the Zernike models within the A-projection framework. As mentioned earlier, this branch currently only corrects for Mueller-diagonal terms, and the full Mueller corrections are underway. We will present the details of both the aperture and image plane wide-field polarization leakage corrections in a forthcoming paper in this series (Jagannathan et al., 2021, in preparation).

The National Radio Astronomy Observatory is a facility of the National Science Foundation operated under cooperative agreement by Associated Universities, Inc. The MeerKAT telescope is operated by the South African Radio Astronomy Observatory, which is a facility of the National Research Foundation, an agency of the Department of Science and Innovation. IDIA is a partnership of the University of Cape Town, the University of Pretoria and the University of the Western Cape. We acknowledge the use of the ilifu cloud computing facility -www.ilifu.ac.za a partnership between the University of Cape Town, the University of the Western Cape,

[6] https://github.com/ARDG-NRAO/plumber

the University of Stellenbosch, Sol Plaatje University, the Cape Peninsula University of Technology and the South African Radio Astronomy Observatory. The ilifu facility is supported by contributions from IDIA, the Computational Biology division at UCT and the Data Intensive Research Initiative of South Africa (DIRISA).

This paper makes use of the following ALMA data: *uid___A002_Xd2d9a0_X8dd3*, *uid___A002_Xd2d9a0_X92ae*, *uid___A002_Xd2d9a0_X991e*, *uid___A002_Xd2d9a0_X8f4c*, *uid___A002_Xd2d9a0_X9427*, *uid___A002_Xd2d9a0_X9b2e*. ALMA is a partnership of ESO (representing its member states), NSF (USA) and NINS (Japan), together with NRC (Canada), MOST and ASIAA (Taiwan), and KASI (Republic of Korea), in cooperation with the Republic of Chile. The Joint ALMA Observatory is operated by ESO, AUI/NRAO and NAOJ.

S.S. acknowledges financial support from the Inter-University Institute for Data Intensive Astronomy (IDIA) and the National Radio Astronomy Observatory (NRAO). IDIA is a partnership of the University of Cape Town, the University of Pretoria, and the University of the Western Cape. P.J. would like to thank Bruce Veidt and Tom Landecker for interesting discussions about the modeling of aperture illumination functions.

Facilities: VLA, ALMA, MeerKAT, ilifu .

Appendix A
FM Models

Figure 12 plots the full Mueller models for all the telescopes discussed in this paper. These models were obtained by constructing the Mueller elements from the Jones models.

Appendix B
Implementation of Zernike Coefficients in `tclean`

The coefficients derived in the manner described in Section 2.4 are included in the `awproject` gridder in CASA by listing them in a CSV file. This format allows for the specification of Zernike coefficients as a function of frequency, polarization, and antenna type (when necessary). Each band of each telescope will be specified in a different CSV file that can be passed into the code. Listing 1 shows an extract of such a CSV file. This is an extendable format that can be modified to accept heterogeneous arrays (partially or fully) by adding a further index to track the antenna type.

Listing 1—Extract from the CSV file specifying the cofficients for the VLA *S*-Band beams. The columns are Stokes, frequency (in MHz), the Zernike index, the real and imaginary coefficients, and the aperture efficiency factor. The Stokes is listed in CASA readable format, using the numbers 5–8 to denote circular feeds and 9–12 for linear.

```
#stokes,freq,ind,real,imag,eta
5,2052,0,308.13023030,-0.06968780,1.11
6,2052,0,0.14375480,-0.07500360,1.11
7,2052,0,0.11308890,0.24478490,1.11
8,2052,0,301.83666030,-0.00622780,1.11
```

Since Zernike polynomials are analytically well defined, and the aperture models can be exactly evaluated at the specified UV locations during gridding, rather than using a cached precomputed value from an oversampled grid.

ORCID iDs

Srikrishna Sekhar https://orcid.org/0000-0002-8418-9001
Preshanth Jagannathan https://orcid.org/0000-0002-5825-9635
Brian Kirk https://orcid.org/0000-0002-7753-9130
Sanjay Bhatnagar https://orcid.org/0000-0001-7164-0089

References

Asad, K. M. B., Girard, J. N., de Villiers, M., et al. 2021, MNRAS, 502, 2970
Bates, R. 1971, IJES, 9, 1107
Bhatnagar, S., & Cornwell, T. 2017, AJ, 154, 197
Bhatnagar, S., Cornwell, T., Golap, K., & Uson, J. M. 2008, A&A, 487, 419
Bhatnagar, S., Jagannathan, P., Sekhar, S., et al. 2020, ALMA Study Project Report: Full Mueller Mosaic Imaging with ALMA, National Radio Astronomy Observatory https://science.nrao.edu/facilities/alma/science_sustainability/Bhatnagar_FMImagingALMA.pdf
Bhatnagar, S., Rau, U., & Golap, K. 2013, ApJ, 770, 91
Born, M., & Wolf, E. 2013, Principles of Optics: Electromagnetic Theory of Propagation, Interference and Diffraction of Light (Amsterdam: Elsevier)
Branch, M. A., Coleman, T. F., & Li, Y. 1999, SIAM J. Sci. Comput., 21, 1
Cornwell, T. J., Golap, K., & Bhatnagar, S. 2008, ISTSP, 2, 647
Cotton, W. D., Condon, J. J., Perley, R. A., et al. 2004, Proc. SPIE, 5489, 180
Du, X., Landecker, T. L., Robishaw, T., et al. 2016, PASP, 128, 115006
Esterhuyse, W., Kusel, T., Theron, I., et al. 2011, Concept Description: MeerKAT Receptor for Consideration by SKA Technical Report WP2-020.045.010-TD-005, Square Kilometre Array https://www.skatelescope.org/public/2011-07-13_Dish_Array_CoDR/WP2-020.045.010-TD-005-A_MKreceptor.pdf
Hamaker, J., Bregman, J., & Sault, R. 1996, A&AS, 117, 137
Intema, H. T., Van der Tol, S, Cotton, WD, Cohen, AS, Van Bemmel, IM, & R{\"o}ttgering, HJA 2009, A&A, 501, 1185
Jagannathan, P., Bhatnagar, S., Brisken, W., & Taylor, A. R. 2018, AJ, 155, 3
Jagannathan, P., Bhatnagar, S., Rau, U., & Taylor, A. R. 2017, AJ, 154, 56
Jonas, J., & Team, MeerKAT 2018, in Proc. of MeerKAT Science: On the Pathway to the SKA, 25, ed. Russ Taylor, Prof et al. (Trieste: SISSA) https://pos.sissa.it/277/
Lakshminarayanan, V., & Fleck, A. 2011, JMOp, 58, 545
McMullin, J. P., Waters, B., Schiebel, D., Young, W., & Golap, K. 2007, in ASP. Conf. Ser. 376, Astronomical Data Analysis Software and Systems XVI, ed. R. A. Shaw, F. Hill, & D. J. Bell (San Francisco, CA: ASP), 127
Moré, J. J. 1978, Numerical Analysis (Berlin: Springer), 105
Napier, P., & Bates, R. 1971, IJES, 9, 1193
Noll, R. J. 1976, JOsA, 66, 207
Noordam, J. E. 2004, Proc. SPIE, 5489, 817
Perley, R. 2016, Jansky Very Large Array Primary Beam Characteristics EVLA Memo 195, National Radio Astronomy Observatory https://library.nrao.edu/public/memos/evla/EVLAM_195.pdf
Perley, R., Chandler, C., Butler, B., & Wrobel, J. 2011, ApJL, 739, L1
Rau, U., Bhatnagar, S., & Owen, F. N. 2016, AJ, 152, 124
Rau, U., Bhatnagar, S., Voronkov, M. A., & Cornwell, T. J. 2009, IEEEP, 97, 1472
Robitaille, T. P., Tollerud, E. J., Greenfield, P., et al. 2013, A&A, 558, A33
Scott, P. F., & Ryle, M. 1977, MNRAS, 178, 539
Sekhar, S., & Jagannathan, P. 2021a, ZCPB, V1.0, Zenodo, doi:10.5281/zenodo.5484156
Sekhar, S., & Jagannathan, P. 2021b, Plumber, v0.1, Zenodo, doi:10.5281/zenodo.5484098
Sokolowski, M., Colegate, T., Sutinjo, A., et al. 2017, PASA, 34, E062
Tasse, C., Van Der Tol, S., Van Zwieten, J., van Diepen, G., & Bhatnagar, S. 2013, A&A, 553, A105
Van der Tol, S., Veenboer, B., & Offringa, A. R. 2018, A&A, 616, A27
Van Weeren, R., Williams, W., Hardcastle, M., et al. 2016, ApJS, 223, 2
Virtanen, P., Gommers, R., Oliphant, T. E., et al. 2020, NatMe, 17, 261
Wootten, A. 2003, Proc. SPIE, 4837, 110
Zernike, F. 1934, MNRAS, 94, 377